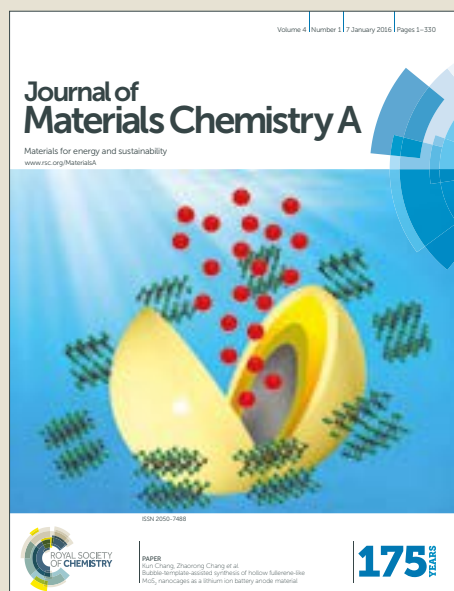


# Journal of Materials Chemistry A

Accepted Manuscript



This article can be cited before page numbers have been issued, to do this please use: Y. Zhao, J. Liang, Q. Sun, L. Goncharova, J. Wang, C. Wang, K. Adair, X. Li, F. Zhao, Y. Sun, R. Li and X. Sun, *J. Mater. Chem. A*, 2019, DOI: 10.1039/C8TA10174D.



This is an Accepted Manuscript, which has been through the Royal Society of Chemistry peer review process and has been accepted for publication.

Accepted Manuscripts are published online shortly after acceptance, before technical editing, formatting and proof reading. Using this free service, authors can make their results available to the community, in citable form, before we publish the edited article. We will replace this Accepted Manuscript with the edited and formatted Advance Article as soon as it is available.

You can find more information about Accepted Manuscripts in the [author guidelines](#).

Please note that technical editing may introduce minor changes to the text and/or graphics, which may alter content. The journal's standard [Terms & Conditions](#) and the ethical guidelines, outlined in our [author and reviewer resource centre](#), still apply. In no event shall the Royal Society of Chemistry be held responsible for any errors or omissions in this Accepted Manuscript or any consequences arising from the use of any information it contains.

# In-situ Formation of Highly Controllable and Stable Na<sub>3</sub>PS<sub>4</sub> as Protective Layer for Na Metal Anode

Yang Zhao<sup>1+</sup>, Jianwen Liang<sup>1+</sup>, Qian Sun<sup>1</sup>, Lyudmila V. Goncharova<sup>2</sup>, Jiwei Wang<sup>1</sup>, Changhong Wang<sup>1</sup>, Keegan R Adair<sup>1</sup>, Xiaona Li<sup>1</sup>, Feipeng Zhao<sup>1</sup>, Yipeng Sun<sup>1</sup>, Ruying Li<sup>1</sup>, Xueliang Sun<sup>1\*</sup>

<sup>1</sup> Department of Mechanical and Materials Engineering  
University of Western Ontario, London, Ontario, N6A 5B9, Canada

\*E-mail: xsun@eng.uwo.ca (X.L. Sun)

<sup>2</sup> Department of Physics and Astronomy  
University of Western Ontario, London, Ontario, N6A 3K7, Canada

+ These authors contributed equally to this work.

## Abstract

Na metal is considered as a promising anode material for Na-ion batteries (NIBs) and Na metal batteries (NMBs) due to its high theoretical specific capacity and low electrochemical potential. However, the Na metal anode faces several challenges, including: (1) safety concerns related to dendrite formation (2) low Coulombic efficiency (CE) and poor cycling performance caused by unstable solid electrolyte interphase (SEI); and (3) an infinite volume change due to its hostless nature. In this paper, we demonstrate for the first time a facile and in-situ solution-based method to synthesize an artificial protective layer of  $\text{Na}_3\text{PS}_4$  (NaPS) on the surface of Na metal. Promisingly, the thickness and composition of the NaPS can be controlled through adjustment of the precursor concentration and reaction times. The thin amorphous NaPS layers on the surface of the Na metal will reduce parasitic side reactions with electrolyte components, increase the homogeneity of the SEI layer and improve the  $\text{Na}^+$  flux to the surface. Meanwhile, the ionically conductive NaPS can eliminate the strong electric field buildup at the surface, resulting in a more homogeneous Na plating/stripping process with suppressed Na dendrite growth. The design of the NaPS-coated Na anode opens up new opportunities for the realization of next-generation high-energy density Na metal batteries.

## Introduction

Na-ion batteries (NIBs) and Na metal batteries (NMBs) are considered as promising alternatives to the conventional Li-ion batteries for large-scale energy storage applications due to the wide availability and low cost of sodium sources<sup>1</sup>. In addition, NMBs, including room temperature Na-S and Na-air batteries, show high theoretical specific energy densities of 1274 Wh kg<sup>-1</sup> and 1605 Wh kg<sup>-1</sup>, respectively<sup>2, 3</sup>. Metallic Na is the ultimate choice among all the possible anode candidates due to its high theoretical capacity and low electrochemical potential<sup>4</sup>. However, metallic Na suffers from several challenges during electrochemical cycling, including: 1) The high reactivity between Na and liquid electrolyte causes the formation of a solid electrolyte interphase (SEI) on the surface of Na metal. The unstable SEI layers lead to continuous consumption of liquid electrolyte and shortening of the cycling life time<sup>5</sup>. 2) The inhomogeneous ionic flux on the surface of Na will result in mossy or dendritic Na growth, which can further lead to the formation of “dead Na”, lower the Coulombic efficiency (CE) and cause safety concerns due to the risk of dendrite growth and short-circuiting<sup>6</sup>. 3) The hostless nature of the Na metal anode results in large volume changes during repetitive Na plating/stripping processes<sup>7-9</sup>.

To date, different approaches have been proposed to address the aforementioned challenges of metallic Na, including electrolyte modifications, the design 3D hosts and current collectors, and surface coating/modifications<sup>10-21, 31-32</sup>. In previous studies, it has been demonstrated that using ultra-concentrated electrolytes or additives such as fluoroethylene carbonate (FEC) can stabilize the SEI layer and reduce dendrite growth<sup>22, 23</sup>. Alternatively, surface coating/modification is another effective strategy to achieve stable artificial SEI layers which can suppress Na dendrite growth and increase the life time of NMBs<sup>24-26</sup>. In our previous studies, we demonstrated inorganic Al<sub>2</sub>O<sub>3</sub> and organic-inorganic hybrid alucone (Al- ethylene glycol) thin films as protective layers

for Na metal anodes, achieving enhanced electrochemical stability and cycling life in the ether-based and carbonate-based electrolytes, respectively<sup>27, 28</sup>. In order to achieve ideal artificial SEI layers, a high ionic conductivity coating which can lead to the uniform distribution of ion flux and localized current densities should be developed. Recently, Nazar's group described an efficient way to stabilize Li plating using the Li<sup>+</sup> ion solid electrolyte Li<sub>3</sub>PS<sub>4</sub> as a surface modification for Li metal anodes<sup>29</sup>. The Li<sub>3</sub>PS<sub>4</sub> layer was chemically and electrochemically stable over repeated plating/stripping cycles and delivered more stable plating/stripping performances compared to control Li foils. To the best of our knowledge, there are still no reports using Na<sup>+</sup> ion conductive solid-state electrolytes (SSEs) as an artificial protective layer to address the instability and dendrite growth of Na metal anode.

Herein, we demonstrate a facile and in-situ solution-based approach to fabricate the SSEs protective layer of Na<sub>3</sub>PS<sub>4</sub> (NaPS) on the surface of Na metal. Promisingly, the thickness and composition of the NaPS can be controlled through adjustment of the concentrations of the precursors and reaction times. The thin amorphous NaPS layers on the Na (Na@NaPS) will reduce the reactions with the electrolytes and increase homogeneity of the SEI layers and Na<sup>+</sup> flux. Meanwhile, the NaPS protective layer at the surface of Na metal can achieve the homogeneous Na plating/stripping processes, leading to the suppressed Na dendrite growth. Our design of SSE NaPS-coated Na anode opens up new opportunities for the realization of next-generation high energy density Na metal batteries.

## Results and Discussion

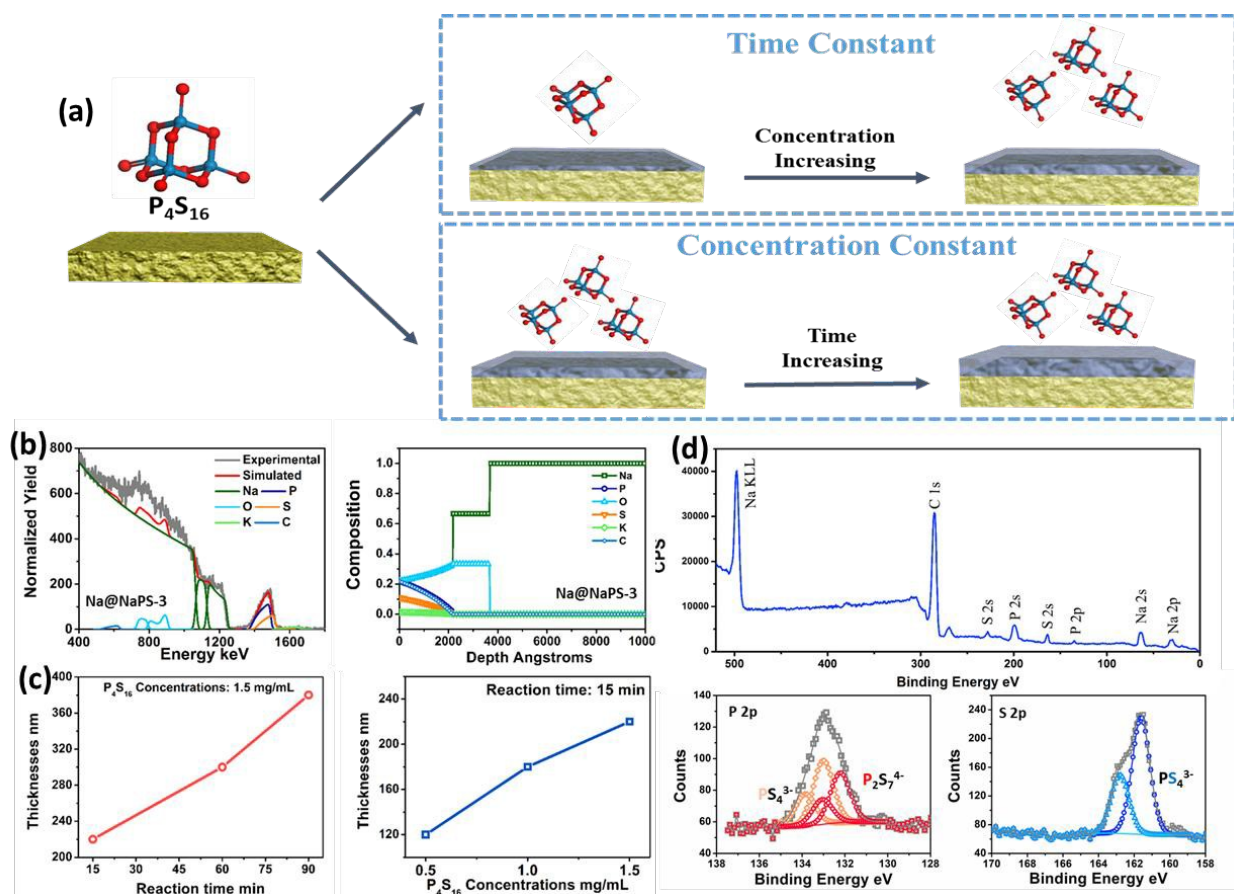


**Figure 1** (a) Schematic diagram of the in-situ fabrication process of NaPS on Na foil; (b) RBS spectra and calculated depth profiles of Na@NaPS-3; (c) the thicknesses of different samples related to the precursor concentrations and reaction times; (d) XPS survey spectra and P 2p and S 2p high-resolution spectra for Na@NaPS-3;

The SSEs NaPS protective layers are formed by a simple in-situ solution-based method. As shown in **Figure 1** (a), sulfur-rich phosphorus sulfide molecules ( $P_4S_{16}$ ) are used as precursors to react with Na metal directly in a diethylene glycol dimethyl ether (DEGDME) solvent. The reaction between Na metal and  $P_4S_{16}$  is shown as:



Due to the high reactivity between Na metal and  $P_4S_{16}$ , the reactions are expected to be controlled with different precursor concentrations and reaction times. The experimental design parameters are shown in **Table S1**. Firstly, the concentrations of the  $P_4S_{16}$  precursor in DEGDME are controlled at  $0.5 \text{ mg mL}^{-1}$ ,  $1 \text{ mg mL}^{-1}$ , and  $1.5 \text{ mg mL}^{-1}$  and used with a constant reaction time of 15 min. The samples in this experiment are named as Na@NaPS-1, Na@NaPS-2 and Na@NaPS-3, respectively. Secondly, the samples with constant concentrations of  $1.5 \text{ mg mL}^{-1}$  are used to study the effect of longer reaction times (60 min and 90 min), and these samples are named as Na@NaPS-4 and Na@NaPS-5, respectively.

Rutherford backscattering spectrometry (RBS) measurements were performed on Na@NaPS-1 to Na@NaPS-5 to confirm the film thicknesses on the Na and deduce the elemental depth profiles. **Figure 1(b)** shows the RBS spectrum and simulated depth profiles for Na@NaPS-3. The presence of P and S peaks from the surface can confirm the successful synthesis of the NaPS films on the Na foil. **Figure S1** show the RBS spectrums and simulated depth profiles for another samples of Na@NaPS-1 (a), Na@NaPS-2 (b), Na@NaPS-4 (c), and Na@NaPS-5 (d). Notably, by increasing the concentration of  $P_4S_{16}$  in DEGDME, the thickness of the NaPS coating increases from 120 nm to 220 nm, as shown in **Figure 1(c)**. Meanwhile, the content of both P and S increase as well (**Table S2**). When keeping the concentration of  $P_4S_{16}$  constant at  $1.5 \text{ mg mL}^{-1}$ , the RBS results indicate that the ratio of Na to P and S stays constant and the thicknesses increase to 300 and 380 nm for Na@NaPS-4 and Na@NaPS-5 with increasing reaction times (**Figure 1 (c)** and **Table S2**). Thus, it can be concluded from the RBS results that the thickness and composition of the NaPS films can be controlled by adjusting the concentration of  $P_4S_{16}$  and reaction times.

To further confirm the chemical compositions of the NaPS films, X-ray photoelectron spectroscopy (XPS) was carried out for typical samples of  $P_4S_{16}$ , Na@NaPS-1, Na@NaPS-3 and

Na@NaPS-5. **Figure S3** (a) and (b) shows the high-resolution XPS spectrum of S 2p and P 2p for the  $P_4S_{16}$ , respectively. The peaks of S  $2p_{1/2}$  and  $2p_{3/2}$  at 164.8 eV and 163.6 eV corresponds to the P-S-P bonding in  $P_4S_{16}$ . Meanwhile, the peaks of P  $2p_{1/2}$  and  $2p_{3/2}$  at 135.2 eV and 134.4 eV can be assigned to the P-S in  $P_4S_{16}$ . **Figure 1(d)** and **Figure S2** present the XPS survey spectra for Na@NaPS-1, Na@NaPS-3 and Na@NaPS-5, where the S and P peaks can be obviously observed, consistent with the RBS results. From the high-resolution P 2p spectra for Na@NaPS-3, several peaks in the high-resolution P 2p spectra can be fitted with different distinct doublets. The double peaks of P  $2p_{1/2}$  and  $2p_{3/2}$  at 133.8 eV and 133.0 eV can be assigned to phosphorous in  $PS_4^{3-29}$ . Meanwhile, the peaks at 133.0 eV and 132.21 eV is related to the bond of P-S in  $P_2S_7^{4-30,31}$ . The XPS results indicate that the content of  $PS_4$  and  $P_2S_7$  is 56 % and 44 % for NaPS-3, respectively. In the S 2p spectra, the S  $2p_{1/2}$  and  $2p_{3/2}$  peaks at 162.5 eV and 161.6 eV are responsive with P=S bond in the  $PS_4^{3-}$  species. Very interesting, from the high-resolution P 2p spectra for Na@NaPS-1 (**Figure.S3 (d)**), not only  $PS_4^{3-}$  peak can be observed, but also the un-reacted  $P_4S_{16}$  peak exists, indicating the incomplete reaction between Na and  $P_4S_{16}$  with low concentration of precursor and shorter reaction time. However, the P 2p spectra for Na@NaPS-5 is almost the same with Na@NaPS-3, indicating that the final products of the coating layer is mixed by both  $Na_3PS_4$  and  $Na_4P_2S_7$ . All the XPS results indicate that the  $Na_3PS_4$  films are successfully synthesized on the surface of Na foils through the in-situ solution-based method.

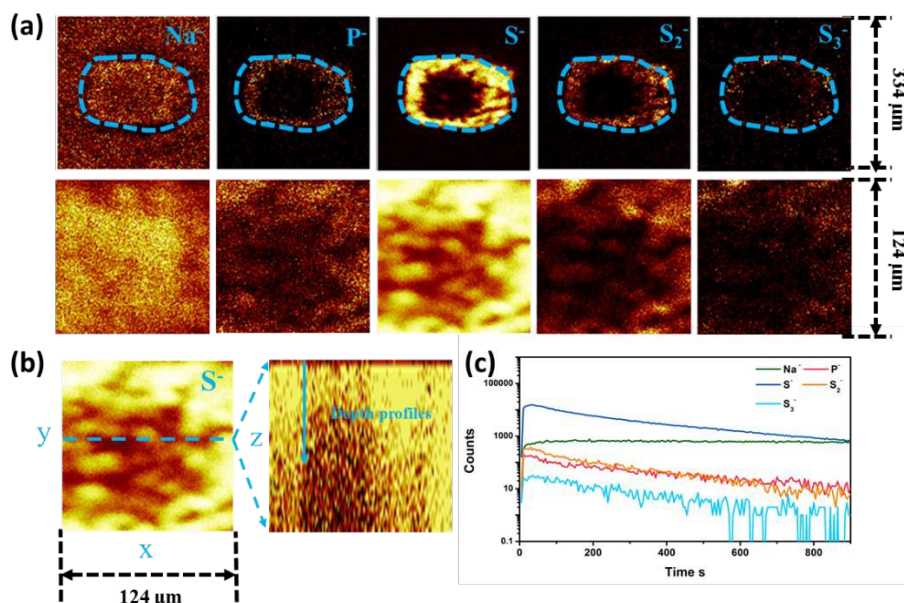


**Figure 2** (a) TOF-SIMS chemical ion images of the  $\text{Na}^+$ ,  $\text{P}^-$ ,  $\text{S}^-$ ,  $\text{S}_2^-$ ,  $\text{S}_3^-$  species for Na@NaPS-3 (Blue circle: sputtering areas); The analysis area was  $300 \times 300 \mu\text{m}^2$  and the sputtering areas of  $100 \times 100 \mu\text{m}^2$ . (b) cross-section ion images of  $\text{S}^-$  species for Na@NaPS-3; (c) TOF-SIMS depth profiles of  $\text{Na}^+$ ,  $\text{P}^-$ ,  $\text{S}^-$ ,  $\text{S}_2^-$ ,  $\text{S}_3^-$  species for Na@NaPS-3.

Time-of-flight secondary ion mass spectrometry (TOF-SIMS) was performed to further probe the compositions of the NaPS film and the element depth distributions. **Figure 2 (a)** shows the secondary ion images of  $\text{Na}^+$ ,  $\text{P}^-$ ,  $\text{S}^-$ ,  $\text{S}_2^-$  and  $\text{S}_3^-$  with the magnified images on the edges after sputtering. Because of the sample exposure to air during the transferring process, the surfaces of the samples are oxidized and no species related to  $\text{Na}_3\text{PS}_4$  films can be observed at the initial stage of analysis. However, after sputtering by  $\text{Cs}^+$  ions, the different negative ions of  $\text{P}^-$ ,  $\text{S}^-$ ,  $\text{S}_2^-$  and  $\text{S}_3^-$  are visible from the edge of the sputtering areas, which are attributed to the  $\text{Na}_3\text{PS}_4$  film on Na foil. **Figure 2(b)** presents cross-section ion images of  $\text{S}^-$  species for Na@NaPS-3, indicating the formation of a continuous  $\text{Na}_3\text{PS}_4$  film from the surface down to the bulk Na. **Figure S4** displays

similar ion images of  $\text{Na}^-$ ,  $\text{P}^-$ ,  $\text{S}^-$ ,  $\text{S}_2^-$  and  $\text{S}_3^-$  for Na@NaPS-1 and Na@NaPS-5, demonstrating the same  $\text{Na}_3\text{PS}_4$  film formed with different experimental conditions. The TOF-SIMS depth profiles of  $\text{Na}^-$ ,  $\text{P}^-$ ,  $\text{S}^-$ ,  $\text{S}_2^-$  and  $\text{S}_3^-$  for Na@NaPS-3 are shown in **Figure 2(c)**. As expected, the signals of  $\text{P}^-$ ,  $\text{S}^-$ ,  $\text{S}_2^-$  and  $\text{S}_3^-$  decrease whereas the signal of  $\text{Na}^-$  remains consistent after 800 s  $\text{Cs}^+$  sputtering. The TOF-SIMS analysis demonstrates that Na (or  $\text{Na}^+$ ) species exists from the surface of the  $\text{Na}_3\text{PS}_4$  coating layer down to the bulk Na metal. **Figure S5** shows the depth profiles of Na@NaPS-1 and Na@NaPS-5, where it can be observe that bulk Na can be reached after sputtering times of 200 s and 1300 s, respectively. The TOF-SIMS analysis further confirms that with increasing concentration of  $\text{P}_4\text{S}_{16}$  and reaction times, the NaPS films grow thicker.

Through combination of characterization techniques such as RBS, XPS and TOF-SIMS, it can be concluded that  $\text{Na}_3\text{PS}_4$  films with controlled thicknesses have been successfully synthesized on Na foil by the in-situ solution-based method. Moreover, from the XRD patterns in **Figure S6**, the as-prepared  $\text{Na}_3\text{PS}_4$  are amorphous without any characteristic XRD signatures. The three main peaks in the XRD patterns are attributed to the cubic Na metal<sup>15</sup>. The morphologies of Na@NaPS-1, Na@NaPS-3 and Na@NaPS-5 are presented in **Figure S7** and **Figure S8**. From the top view SEM images in **Figure S7 (a, b and c, d)**, smooth and continuous films are formed on the surface for both Na@NaPS-1 and Na@NaPS-3. However, a rougher surface with larger particles sizes is obtained with longer reaction time and higher precursor concentration for Na@NaPS-5 (**Figure S7 (e, f)**). From the cross-section SEM images (**Figure S8**), the NaPS layer grows thicker from Na@NaPS-1 to Na@NaPS-5. In brief, the trend of the thickness as the function of the concentration of  $\text{P}_4\text{S}_{16}$  solution and the reaction time is well consistent from the RBS, TOF-SIMS, and SEM results.

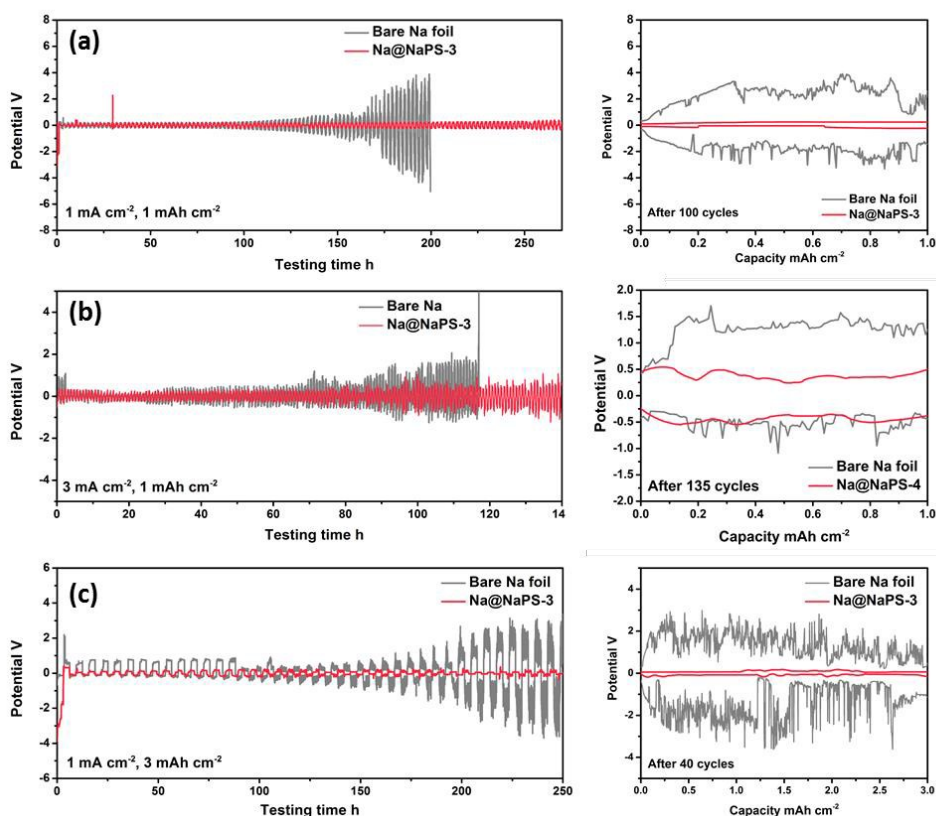


**Figure 3** (a) Comparison of the cycling stability and potential profiles of the Na@NaPS-3 and bare Na foil at a current density of  $1 \text{ mA cm}^{-2}$  with the capacity of  $1 \text{ mAh cm}^{-2}$ ; (b) The cycling stability and potential profiles of the Na@NaPS-3 and bare Na foil at a current density of  $3 \text{ mA cm}^{-2}$  with the capacity of  $1 \text{ mAh cm}^{-2}$ ; (c) The cycling stability and of potential profiles of the Na@NaPS-3 and bare Na foil at a current density of  $1 \text{ mA cm}^{-2}$  with a capacity of  $3 \text{ mAh cm}^{-2}$ .

Galvanostatic cycling of  $\text{Na}_3\text{PS}_4$  coated Na and bare Na foils was studied using a symmetrical cell configuration of Na@NaPS/separators/Na@NaPS, using a 1 M  $\text{NaPF}_6$  electrolyte dissolved in 1:1 (v:v) EC:PC. **Figure 3(a)** presents a comparison of the cycling stability of Na@NaPS-3 and bare Na foil at a current density of  $1 \text{ mA cm}^{-2}$  with a capacity of  $1 \text{ mAh cm}^{-2}$ . The thicknesses effects of NaPS on the electrochemical performances will be discussed in the following part. For

pristine Na foil, the initial stripping/plating over-potential is about 200 mV (versus  $\text{Na}^+/\text{Na}$ ). Subsequently, the over-potential starts to increase after 150 h and reaches 4000 mV after 160 h. It can be observed that the pristine Na foil suffers from unstable voltage profile fluctuations, resulting in short circuiting of the cell. Promisingly, the Na@NaPS-3 delivers the slightly larger over-potential in the first plating process and then stabilizes in the following cycles with an over-potential of 300 mV (versus  $\text{Na}^+/\text{Na}$ ), which can be sustained for more than 270 h. The potential profiles of Na@NaPS-3 and bare Na foil are also shown in **Figure 3(a)**, in which the Na foil displays unstable over-potentials with large polarization and Na@NaPS-3 presents smoother profiles with negligible increase in hysteresis. When increasing the current density to  $3 \text{ mA cm}^{-2}$ , the over-potential of pristine Na is seen to rapidly increase after only 70 h (**Figure 3(b)**). Furthermore, the over-potential reaches over 5000 mV (versus  $\text{Na}^+/\text{Na}$ ) after 115 h, which is the voltage cut-off limitation in the testing. Promisingly, the Na@NaPS-3 maintains improved stability at higher current density with a lower over-potential of 500 mV after 140 h. In the previously reported literatures, the cycling capacity of metal anodes (for both Li and Na metal anode) in symmetrical cell testing is usually around  $1 \text{ mAh cm}^{-2}$  or even lower, which cannot meet the requirements for practical applications. Herein, we also demonstrate the Na@NaPS-3 with a large capacity of  $3 \text{ mAh cm}^{-2}$  compared with bare Na foil under the same testing conditions. **Figure 3(c)** presents the cycling stability and voltage profiles of both Na@NaPS-3 and bare Na foil using the high capacity limit of  $3 \text{ mAh cm}^{-2}$  under the current density of  $1 \text{ mA cm}^{-2}$ . The bare Na foil exhibits unstable plating/stripping behavior after 100 h of cycling with increasing over-potentials which rise to 3000 mV after 180 h (**Figure 3(c)**). However, the Na@NaPS-3 displays a stable cycling performance with an over-potential of only 300 mV after 250 h, which is almost 10 times

lower than what was observed for bare Na foil. Based on these observations, the NaPS coating is an excellent protective layer for Na metal anode in applications that require a large capacity.

To understand the relationships between thickness, composition and electrochemical performance, the other samples of Na@NaPS-1, Na@NaPS-2, and Na@NaPS-4, Na@NaPS-5 were studied under a current density of  $1 \text{ mA cm}^{-2}$  with cycling capacities of  $1 \text{ mAh cm}^{-2}$  and  $3 \text{ mAh cm}^{-2}$ . **Figure S9** shows the electrochemical performances of samples obtained with lower  $\text{P}_4\text{S}_{16}$  concentrations for Na@NaPS-1 and Na@NaPS-2. From the results, it can be seen that both Na@NaPS-1 and Na@NaPS-2 exhibit better performances than that of the bare Na foil, in which the stability of Na@NaPS-2 appears to be enhanced compared to Na@NaPS-1. However, they are still not comparable to Na@NaPS-3. From the discussion above, the NaPS coating becomes thicker with an increase in  $\text{P}_4\text{S}_{16}$  concentration. Furthermore, we find that the thicknesses of the NaPS protective layers have a significant influence on the electrochemical performances. The higher  $\text{P}_4\text{S}_{16}$  concentrations leading to thicker coatings (Na@NaPS-3) shows the best benefits in term of the plating/stripping performances. Furthermore, the cycling stabilities of the samples of Na@NaPS-4, Na@NaPS-5 with longer reactions are presented in **Figure S10**. The performances of Na@NaPS-4 and Na@NaPS-5, appear to be inferior to the bare Na foil. The reason could be explained as: 1) From Figure.S7, a rougher surface with larger particles sizes is obtained with longer reaction time and higher precursor concentration for Na@NaPS-5. The rougher surface with large particles could lead to the nonuniform distribution of the  $\text{Na}^+$  flux during electrochemical cycling, which will aggravate the mossy-like and dendritic Na growth. 2) From the cross-section view SEM images (Figure.S8), it can be observed that NaPS-5 with longer reaction time presents the porous structure for the coating layer compared to NaPS-3. This porous structure of coating layer could still cause the side reactions between the Na metal and liquid electrolyte, leading to

the even worse performances. This result indicates that the coating thickness (from RBS and SIMS results) and surface roughness (from SEM results) are critical parameters and excessive coating can lead to poor electrochemical performances. Thus, the Na@NaPS-3 with the Na<sub>3</sub>PS<sub>4</sub> layer of ~220 nm displays the best electrochemical performances with respect to cycling current density and capacity.

The performance of the bare Na foil and Na@NaPS-3 as anodes for NMBs was further investigated in a full cell using a NaCrO<sub>2</sub>/C cathode. The loading of NaCrO<sub>2</sub>/C is ~ 8 mg cm<sup>-2</sup> corresponding to an areal capacity of ~1.1 mAh cm<sup>-2</sup>. **Figure S11** presents the cycling performances of full cells using bare Na foil and Na@NaPS-3 as the anode at a rate of 1 C (~ 1.1 mA cm<sup>-2</sup>). In the batteries using bare Na foil, the specific capacity drops to 35 mAh g<sup>-1</sup> after 75 cycles due to the poor cyclability of the planar Na foil. Promisingly, the Na@NaPS-3 anode can enable full cells that can maintain a stable capacity of 106 mAh g<sup>-1</sup> over 75 cycles. The cycling stability and capacity retention demonstrates that the NaPS protective layer can effectively improve the electrochemical performances compared to the Na foil in a full cell format.

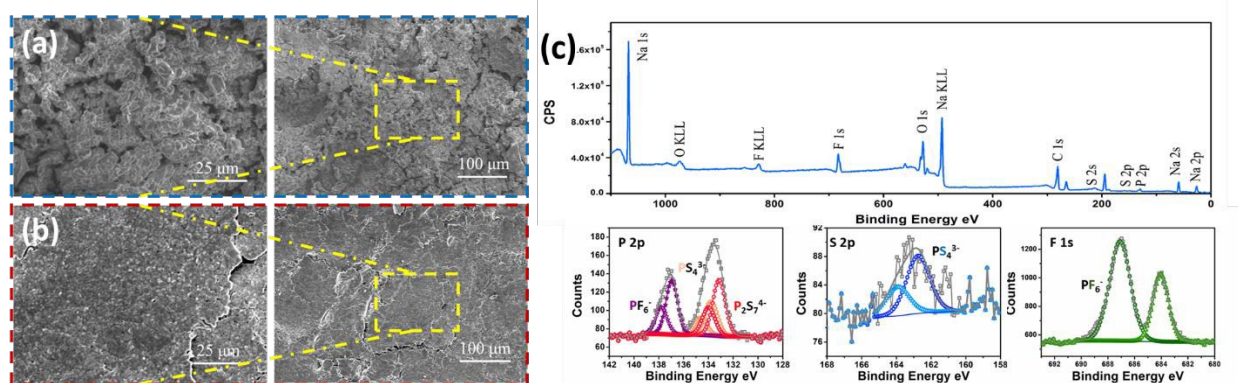


**Figure 4** Top-view SEM images of the bare Na foil (a) and Na@NaPS-3 (b) after 10 cycles of stripping/plating; (c) XPS spectra and P 2p, S 2p and F 1s spectrum of Na@NaPS-3 after cycling.

In order to understand the enhanced performance of NaPS-coated Na anode compared to the pristine Na foil, the morphologies of Na@NaPS-3 and Na foil after cycling were analyzed by SEM. **Figure 4(a, b)** compares the SEM images of Na@NaPS-3 and Na foil after 10 cycles of electrochemical plating/stripping at a current density of  $1 \text{ mA cm}^{-2}$  with the capacity limit of  $1 \text{ mAh cm}^{-2}$ . From the SEM images shown in **Figure 4(a)**, Na dendrites with moss-like structures of approximately  $10\text{-}20 \text{ }\mu\text{m}$  can be clearly observed for bare Na foil after cycling. Meanwhile, the surface of the Na foil becomes very rough and porous with the formations of dead Na. These types of moss/dendritic Na will further lead to the formation of dead sodium during the plating/stripping process, which will decrease CE and consume active Na as well as electrolyte. More SEM images of Na foil after cycling are shown in **Figure S12**. Large moss-like and porous dead Na particles are observed from different areas on the Na foil. Promisingly, with the NaPS coating layers, the surface morphology of Na after electrochemical plating/stripping is relatively smooth and does not possess any high surface area porous structures, as shown in **Figure 3(b)**. The flake-like coating layers can be clearly seen from the surface of Na@NaPS-3, indicating that the NaPS protective layers remain after cycling. **Figure S12** (e-g) displays similar SEM images of Na@NaPS-3 after cycling from another area of the electrode demonstrating the relatively uniform and smooth surface enabled by the NaPS protection layers.

XPS testing was performed to determine the surface chemical nature of Na foil and Na@NaPS-3 electrodes after electrochemical plating and stripping. The full XPS spectra and high resolution XPS spectrum of P 2p, S 2p and F 1s of Na@NaPS-3 after cycling is shown in **Figure 4 (c)**. From the full XPS spectra, Both S 2p and P 2p peaks arising from the NaPS film can be observed after cycling. In the F 1s spectrum, the peak at  $686 \text{ eV}$  is due to residual  $\text{Na}_x\text{PF}_y$  and  $\text{Na}_x\text{PO}_y\text{F}_z$  generated from electrolyte on the surface, which is consistent with the peaks at  $137 \text{ eV}$

for the P 2p spectrum. It is apparent that both the S 2p and P 2p peaks are similar to that of the spectrum from the original Na@NaPS-3 samples in **Figure 1**, which are attributed to the characteristic signal of  $\text{PS}_4^{3-}$  in the  $\text{Na}_3\text{PS}_4$  films. The XPS results show that the NaPS protective layers are very robust and can retain its structure after electrochemical cycling.

Furthermore, TOF-SIMS was employed to study the surface and elemental depth distributions of Na@NaPS-3 after cycling. **Figure S14** show the ion images of  $\text{Na}^-$ ,  $\text{P}^-$ ,  $\text{S}^-$  and  $\text{S}_2^-$  of Na@NaPS-3 after electrochemical cycling (images before and after depth profile sputtering). From the ion images before depth profile sputtering, signals arising from  $\text{P}^-$  and  $\text{S}^-$  species are seen to be distributed uniformly on the surface. After sputtering by  $\text{Cs}^+$  ions, the different negative ions of  $\text{P}^-$ ,  $\text{S}^-$ ,  $\text{S}_2^-$  present stronger signals from the edge of the sputtering areas, indicating the NaPS film is electrochemically stable and remains intact. **Figure 4 (e)** shows the depth profiles of  $\text{F}^-$ ,  $\text{Na}^-$ ,  $\text{P}^-$ ,  $\text{S}^-$ ,  $\text{S}_2^-$  and  $\text{PF}_6^-$  for Na@NaPS-3 after cycling. Combined with the ion images in **Figure S15** of  $\text{F}^-$  and  $\text{PF}_6^-$ , the top surface of the Na@NaPS-3 after cycling is covered with the salt of  $\text{NaPF}_6$ , which is also consistent with XPS results. After sputtering, the  $\text{NaPF}_6$  is almost completely removed and the signal of other species of  $\text{P}^-$ ,  $\text{S}^-$  and  $\text{S}_2^-$  significantly increase. After 350 s, the concentration of  $\text{P}^-$ ,  $\text{S}^-$ , and  $\text{S}_2^-$  ions from the NaPS film decrease, indicating that the thickness of the NaPS film has a very small change after cycling when compared with the profiles in **Figure 2(c)**.

In conclusion, we firstly demonstrate a facile and in-situ solution-based method to fabricate a solid-state electrolyte  $\text{Na}_3\text{PS}_4$  protective layer on the Na metal anode for long life Na metal batteries. The thickness and chemical composition of the NaPS layers can be controlled by adjusting the precursor concentrations and reaction times, and has been optimized in our study. By protecting the Na foil with  $\text{Na}_3\text{PS}_4$ , the mossy and dendrite-like Na growth is effectively suppressed. From the symmetric cell testing, Na@NaPS-3 displays the most stable electrochemical

performances with lower polarization compared with Na foil. Meanwhile, the optimized Na@NaPS-3 can achieve much better performances with the large capacities and current densities required for practical applications. It is believed that our design of Na<sub>3</sub>PS<sub>4</sub>-coated Na anode can open up new opportunities for the realization of next-generation high energy density Na metal batteries.

## Acknowledgements

X. Sun conceived the overall project. Y. Zhao, J. Liang and Q. Sun designed the experiments. Y.Z. performed and completed the experiments and data analysis and wrote the manuscript. L. Goncharova helped on the RBS testing and analysis. J. Wang and C. Wang carried out the full cell testing. F. Zhao and Y. Sun performed the physical characterizations. K. Adair, X. Li and R. Li interpreted the results and data analysis. All authors read and commented on the manuscript. This research was supported by the Natural Science and Engineering Research Council of Canada (NSERC), the Canada Research Chair Program (CRC), the Canada Foundation for Innovation (CFI), and the University of Western Ontario (UWO). We gratefully acknowledge Dr. Heng-Yong Nie for his help in the discussion on TOF-SIMS results. We would like to acknowledge the technical expertise of Mr. Jack Hendriks at Western Tandetron accelerator facility.

## Reference

1. Hwang, J. Y.; Myung, S. T.; Sun, Y. K. *Chemical Society reviews* **2017**, 46, (12), 3529-3614.
2. Yadegari, H.; Norouzi Banis, M.; Lushington, A.; Sun, Q.; Li, R.; Sham, T.-K.; Sun, X. *Energy Environ. Sci.* **2017**, 10, (1), 286-295.
3. Yadegari, H.; Li, Y.; Banis, M. N.; Li, X.; Wang, B.; Sun, Q.; Li, R.; Sham, T.-K.; Cui, X.; Sun, X. *Energy Environ. Sci.* **2014**, 7, (11), 3747-3757.
4. Cheng, X. B.; Zhang, R.; Zhao, C. Z.; Zhang, Q. *Chemical Reviews* **2017**, 117, (15), 10403–10473

5. Wei, S.; Choudhury, S.; Tu, Z.; Zhang, K.; Archer, L. A. *Accounts of Chemical Research* **2018**, 51, (1), 80-88.
6. Luo, W.; Hu, L. *ACS Central Science* **2015**, 1, (8), 420-2.
7. Lin, D.; Liu, Y.; Cui, Y. *Nature nanotechnology* **2017**, 12, (3), 194-206.
8. Zhang, R.; Li, N. W.; Cheng, X. B.; Yin, Y. X.; Zhang, Q.; Guo, Y. G. *Advanced Science* **2017**, 4, (3), 1600445.
9. Zhao, Y.; Goncharova, L. V.; Sun, Q.; Li, X.; Lushington, A.; Wang, B.; Li, R.; Dai, F.; Cai, M.; Sun, X. *Small Methods* **2018**, 1700417.
10. Seh, Z. W.; Sun, J.; Sun, Y.; Cui, Y. *ACS central science* **2015**, 1, (8), 449-55.
11. Zheng, J.; Chen, S.; Zhao, W.; Song, J.; Engelhard, M. H.; Zhang, J.-G. *ACS Energy Letters* **2018**, 3, (2), 315-321.
12. Ruiz-Martínez, D.; Kovacs, A.; Gómez, R. *Energy & Environmental Science* **2017**, 10, (9), 1936-1941.
13. Wei, S.; Choudhury, S.; Xu, J.; Nath, P.; Tu, Z.; Archer, L. A. *Advanced materials* **2017**, 29, (12) 1605512
14. Kim, Y. J.; Lee, H.; Noh, H.; Lee, J.; Kim, S.; Ryou, M. H.; Lee, Y. M.; Kim, H. T. *ACS applied materials & interfaces* **2017**, 9, (7), 6000-6006.
15. Luo, W.; Zhang, Y.; Xu, S.; Dai, J.; Hitz, E.; Li, Y.; Yang, C.; Chen, C.; Liu, B.; Hu, L. *Nano letters* **2017**, 17, (6), 3792-3797.
16. Cohn, A. P.; Muralidharan, N.; Carter, R.; Share, K.; Pint, C. L. *Nano letters* **2017**, 17, (2), 1296-1301.
17. Liu, S.; Tang, S.; Zhang, X.; Wang, A.; Yang, Q. H.; Luo, J. *Nano letters* **2017**, 17, (9), 5862-5868.
18. Lu, Y.; Zhang, Q.; Han, M.; Chen, J. *Chemical communications* **2017**, 53, (96), 12910-12913.
19. Xu, Y.; Menon, A. S.; Harks, P. P. R. M. L.; Hermes, D. C.; Haverkate, L. A.; Unnikrishnan, S.; Mulder, F. M. *Energy Storage Materials* **2018**, 12, 69-78.
20. Zhao, Y.; Yang, X.; Kuo, L. Y.; Kaghazchi, P.; Sun, Q.; Liang, J.; Wang, B.; Lushington, A.; Li, R.; Zhang, H.; Sun, X. *Small* **2018**, 14, (20), 1703717.
21. Zhao, Y.; Adair, K. R.; Sun, X. *Energy & Environmental Science* **2018**, DOI:10.1039/C8EE01373J
22. Dugas, R.; Ponrouch, A.; Gachot, G.; David, R.; Palacin, M. R.; Tarascon, J. M. *Journal of The Electrochemical Society* **2016**, 163, (10), A2333-A2339.
23. Lee, J.; Lee, Y.; Lee, J.; Lee, S. M.; Choi, J. H.; Kim, H.; Kwon, M. S.; Kang, K.; Lee, K. T.; Choi, N. S. *ACS applied materials & interfaces* **2017**, 9, (4), 3723-3732.
24. Choudhury, S.; Wei, S.; Ozhaves, Y.; Gunceler, D.; Zachman, M. J.; Tu, Z.; Shin, J. H.; Nath, P.; Agrawal, A.; Kourkoutis, L. F.; Arias, T. A.; Archer, L. A. *Nature communications* **2017**, 8, (1), 898.
25. Luo, W.; Lin, C.-F.; Zhao, O.; Noked, M.; Zhang, Y.; Rubloff, G. W.; Hu, L. *Advanced Energy Materials* **2017**, 7, (2), 1601526.
26. Wang, H.; Wang, C.; Matios, E.; Li, W. *Nano letters* **2017**, 17, (11), 6808-6815.
27. Zhao, Y.; Goncharova, L. V.; Lushington, A.; Sun, Q.; Yadegari, H.; Wang, B.; Xiao, W.; Li, R.; Sun, X. *Advanced materials* **2017**, 29, (18), 1606663
28. Zhao, Y.; Goncharova, L. V.; Zhang, Q.; Kaghazchi, P.; Sun, Q.; Lushington, A.; Wang, B.; Li, R.; Sun, X. *Nano letters* **2017**, 17, (9), 5653-5659.
29. Pang, Q.; Liang, X.; Shyamsunder, A.; Nazar, L. F. *Joule* **2017**, 1, (4), 871-886.

30. Lu, Y.; Gu, S.; Hong, X.; Rui, K.; Huang, X.; Jin, J.; Chen, C.; Yang, J.; Wen, Z. *Energy Storage Materials* **2018**, 11, 16-23.
31. Wenzel, S.; Weber, D. A.; Leichtweiss, T.; Busche, M. R.; Sann, J.; Janek, J. *Solid State Ionics* **2016**, 286, 24-33.
32. C. Wang, H. Wang, E. Matios, X. Hu, W. Li, *Adv. Funct. Mater.* **2018**, 28, 1802282.
33. H. Wang, C. Wang, E. Matios, W. Li, *Angew. Chem. Int. Ed.* **2018**, 57, 7734